

# ML Prediction of Global Ionospheric TEC Maps

Lei Liu<sup>ID</sup>, Y. Jade Morton<sup>ID</sup>, *Fellow, IEEE*, and Yunxiang Liu<sup>ID</sup>

**Abstract**—This paper applies the convolutional long short-term memory (convLSTM)-based machine learning (ML) models to forecast global ionospheric total electron content (TEC) maps with up to 24 hours of lead time at a 1-hour interval. Four convLSTM-based models were investigated, and the one that implements the  $L_1$  loss function and the residual prediction strategy demonstrates the best performance. The convLSTM models are trained and evaluated using Centre for Orbit Determination in Europe (CODE) global TEC maps over a period of nearly seven years from October 19, 2014 to July 21, 2021. Results show that the best convLSTM model outperforms the 1-day predicted global TEC products released by CODE analysis center (c1pg) and persistence models under various levels of solar and geomagnetic activities, except for a lead time beyond 8 hours during the storm time where the c1pg has slightly better performance. The convLSTM forecasting performance degrades as the lead time increases.

**Index Terms**—Ionospheric total electron content (TEC), machine learning (ML) prediction, convolutional long short-term memory (convLSTM)

## I. INTRODUCTION

IONOSPHERIC total electron content (TEC) refers to the total number of electrons integrated along a radio wave propagation path within a unit cross section area (unit: TECU,  $1\text{TECU}=10^{16}\text{electrons}/m^2$ ). Satellite navigation and radio communication system performance are degraded when radio waves traverse the ionosphere in the presence of the ionospheric TEC gradients and plasma density irregularities [1], [2], [3]. Reliable specification and prediction of ionospheric TEC are not only helpful for mitigating uncertainties in global navigation satellite system (GNSS)-based position, navigation, and timing (PNT) services, but also for timely warning of space weather activities [4], [5], [6].

Ionospheric TEC maps can be constructed using networks of dual-frequency GNSS receiver measurements [7], [8], [9], [10]. A major challenge is to forecast global TEC maps accurately, especially for relatively long lead times such as one day. This is due to the ionospheric dynamic nature driven by solar-geomagnetic activities and multi-scale ionospheric processes [11], [12], [13], [14]. Numerous approaches have been developed to forecast global ionospheric TEC maps. For example, Schaer [7] presented the least square collocation method to extrapolate spherical harmonic (SH) coefficients that were used for constructing TEC maps. The resulting global TEC maps are one of the international GNSS service

(IGS) official ionospheric products released by the Centre for Orbit Determination in Europe (CODE). García-Rigo et al. [15] developed a global TEC prediction model based on the discrete cosine transform. Wang et al. [16] developed an adaptive autoregressive model to predict the SH coefficients and reproduce the global TEC map by using the predicted SH coefficients.

In recent years, machine learning (ML) techniques have become a promising and effective tool to predict global TEC maps. For example, Perez [17] predicted global ionospheric TEC based on a fully connected neural network (NN). The model was evaluated by the position error in GNSS single frequency ionospheric delay correction. However, the equatorial ionization anomalies (EIA) were not well captured by the predicted global TEC maps. Lee et al. [18] predicted daily global TEC maps with a 2-hour interval using an image-based conditional generative adversarial network (GAN). The results demonstrated that the model had slightly better performance compared to the CODE prediction products. However, this performance comparison may not be fair because the training data used in Lee et al. [18] was obtained from the IGS final TEC products that are weighted mean TEC values of four ionospheric analysis centers (JPL, CODE, ESA and UPC), while the CODE predicted TEC maps are obtained only from the CODE TEC products. Liu et al. [19] applied the long short-term memory (LSTM) network to forecast SH coefficients for the next two hours by incorporating SH coefficients, solar data, and geomagnetic data. The model showed competitive prediction performance compared to traditional models, while further study is still needed to extend its prediction lead time. Boulch et al. [20] presented convolutional recurrent neural networks (RNN) for global ionospheric TEC prediction using CODE TEC data from 2014 to 2016. Their results showed that the prediction performance was comparable with that of the autoregressive (AR), autoregressive moving average (ARMA), and the radial basis function NN.

This paper extends the work of Boulch et al. [20] to implement four variations of an image-based convolutional long short-term memory (convLSTM) ML algorithm to forecast global TEC maps with a lead time up to 24 hours at a 1-hour interval. The CODE TEC maps over a 7-year span from 2014 to 2021 collected under various levels of solar and geomagnetic activities are used in the implementations. The best performing model among the four implementations is selected based on a set of skill scores, and is compared against two conventional prediction models under various levels of solar and geomagnetic conditions to demonstrate the superior performance.

L. Liu, Y. Morton and Y. Liu are with the Ann & H. J. Smead Department of Aerospace Engineering Sciences, University of Colorado Boulder, Boulder, CO, USA. E-mail: lei.liu@colorado.edu, jade.morton@colorado.edu, yuli9721@colorado.edu. This work was supported by DARPA grant #DI 9AC00009

94 Main contributions of this work compared to that of Boulch  
 95 et al. [20] include the use of an extensive global TEC data set  
 96 spanning 7 years, the improved time resolution from 2 hours  
 97 to 1 hour, different data segmentation for training, testing,  
 98 and validation, the prediction of residual TEC maps between  
 99 consecutive days at the same hour, as well as the utilization of  
 100 batch normalization [21] and dropout [22], and comprehensive  
 101 performance evaluations.

102 This paper is organized as follows. Section II describes the  
 103 data used in the study, the specific ML algorithm implemen-  
 104 tations, and evaluation metrics. Section III presents qualitative  
 105 and statistical evaluation. Section IV concludes the study.

## II. DATA AND METHODOLOGY

### A. Data Description

106 Global ionospheric TEC data used in this study are obtained  
 107 from the CODE Global Ionosphere Maps (GIM). CODE's  
 108 GIMs are gridded TEC maps that are represented by the  
 109 spherical harmonic function derived from worldwide ground-  
 110 based GNSS measurements [7]. The temporal resolution of the  
 111 CODE's GIM has been updated from 2 hours to 1 hour since  
 112 October 19, 2014. Figure 1 shows an example of the CODE  
 113 TEC map at 12:00 UT on October 19, 2014. Locations of  
 114 IGS GNSS receivers, from which measurements were used  
 115 to produce this map, are marked by white colored dots. The  
 116 spatial resolution is  $2.5^\circ$  latitude by  $5^\circ$  longitude (71 in  
 117 height by 73 in width). To ease the ML training process, the  
 118 dimension of the TEC map is resized from  $71 \times 73$  to  $73 \times 73$   
 119 by padding zero values over north and south poles. The grid  
 120 size remains  $2.5^\circ \times 5^\circ$ .  
 121

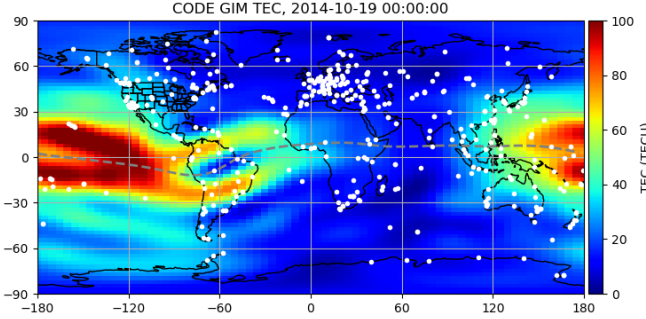


Fig. 1. An example of the global TEC map from the CODE GIM at 12:00 UT on October 19, 2014. White colored dots represent GNSS receivers used to generate the TEC map. The dashed grey line represents the geomagnetic equator. The color scale indicates the value in TECU.

122 The hourly CODE TEC data used in this study are from  
 123 October 19, 2014 to July 21, 2021, which are divided into  
 124 training (60%), validation (20%), and testing (20%) sets.  
 125 To ensure that all three sets of data contain low, moderate,  
 126 and strong solar activity levels and capture seasonal effects,  
 127 we adopt the following novel data segmentation strategy as  
 128 illustrated in Figure 2. The dataset is divided into multiple  
 129 groups, where each group contains 50 days of data. For each  
 130 group (see the bottom panel of Figure 2), the data in the first  
 131 30 days (yellow shaded area) are used for training, and the  
 132 next 10 days (red shaded area) and last 10 days (cyan shaded

134 area) are used for validation and testing, respectively. Based  
 135 on this criteria, 335784, 11760 and 11760 data samples are  
 136 obtained for training, validation, and testing, respectively.

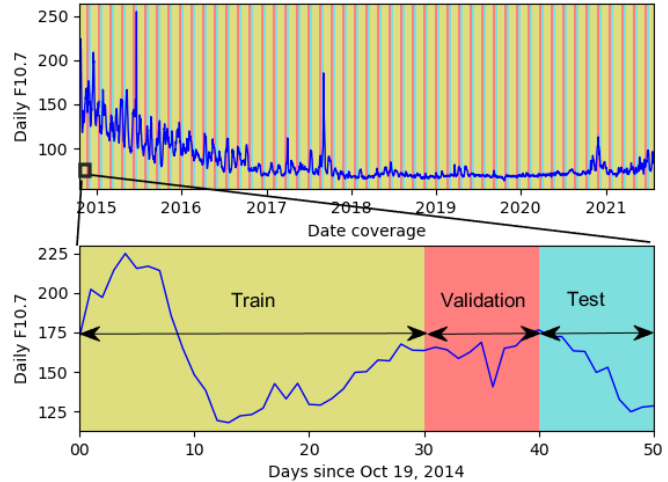


Fig. 2. Top: Data ranging from October 19, 2014 to July 21, 2021 are used. Each group (50 days) in the dataset is divided into training (yellow shaded area), validation (red shaded area) and testing (cyan shaded area) subsets, respectively. Bottom: A close-up view of one group of data starting on Oct 19, 2017. The F10.7 indicator (blue line) shows the daily solar activity level.

### B. convLSTM ML Algorithm

The convLSTM architecture is capable of learning features from a spatiotemporal sequence. It has been successfully applied in many fields of multi-dimensional spatiotemporal predictions [23], [24], [25]. In this study, the convLSTM layer is used as the core module to predict global TEC maps. Detailed structure of the convLSTM module can be found in Figure S1 of the supporting information (SI) file.

Figure 3 illustrates the convLSTM-based ML architecture, which consists of four parts: input, encoder, decoder, and output. The dimensions of the input and output maps are the same ( $73 \times 73$ ). The inputs consist of 24 consecutive TEC maps ( $X_1, X_2, \dots, X_{23}, X_{24}$ ) with a 1-hour interval. These maps are fed into 3 encoder blocks. Each encoder block includes a convolutional (conv) layer and a convLSTM layer. The conv layer and the convLSTM layer are used for down-sampling and learning spatiotemporal features, respectively. Similarly, 3 decoder blocks are composed of deconvolutional (deconv) and convLSTM layers. The hidden features generated by the encoder blocks are used as the inputs for the decoder blocks. The encoder parts are then unfolded using the decoder blocks to predict 24 future maps, which are elements of the output ( $\hat{X}_{25}, \hat{X}_{26}, \dots, \hat{X}_{47}, \hat{X}_{48}$ ) shown in Figure 3. Detailed descriptions of this architecture can be found in Shi et al. [23] and Liu et al. [25]. Here, two prediction strategies are implemented to predict global TEC maps.

- 1) **Residual prediction:** The output ( $\hat{X}_{25}, \hat{X}_{26}, \dots, \hat{X}_{47}, \hat{X}_{48}$ ) is the TEC residual between the map at time  $t$  and  $t-24$ , namely,

$$\hat{X}_t = TEC(t) - TEC(t-24) \quad (1)$$

where  $t=25, 26, \dots, 47, 48$ . Once the TEC residual is produced by the ML model, the predicted TEC map is obtained by adding the background TEC from the previous day to the predicted TEC residual to obtain the predicted TEC.

2) **Direct prediction:** TEC maps are predicted directly by the ML model. This means the model output ( $\hat{X}_{25}, \hat{X}_{26}, \dots, \hat{X}_{47}, \hat{X}_{48}$ ) is the hourly predicted TEC map for the next day.

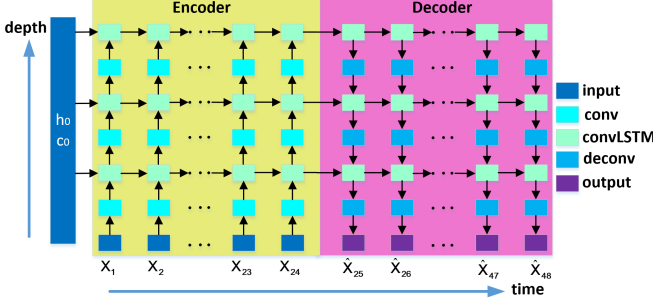


Fig. 3. Illustration of ML architecture. Input:  $X_1, X_2, \dots, X_{23}, X_{24}$  are input TEC maps from the past 24 hours. Output:  $\hat{X}_{25}, \hat{X}_{26}, \dots, \hat{X}_{47}, \hat{X}_{48}$  are 24 predicted targets in the next 24 hours. The targets can be either TEC maps or TEC map residuals, depending on the prediction strategy. Conv: convolutional layer. ConvLSTM: convolutional LSTM layer. Deconv: deconvolutional layer.

The parameter configurations of this architecture, such as filter number, filter size, stride, and padding, as well as the height and width of each output matrix after operations of conv, convLSTM and deconv layers, can be found in Table I.

### C. Evaluation Metrics

To quantify the prediction performance, the following metrics are utilized:

$$\left\{ \begin{array}{l} ME = \frac{1}{N} \sum_{i=1}^N (\hat{x}_i - x_i) \\ RMSE = \sqrt{\frac{1}{N} \sum_{i=1}^N (\hat{x}_i - x_i)^2} \\ CC = \frac{\text{cov}(\hat{x}_i, x_i)}{\sigma_{\hat{x}_i} \cdot \sigma_{x_i}} \end{array} \right. \quad (2)$$

where  $ME$  is the mean error;  $RMSE$  is the root mean square error;  $MAE$  is mean absolute error;  $CC$  is the Pearson correlation coefficient.  $N$  is number of the TEC bins.  $x_i$  and  $\hat{x}_i$  are the gridded TEC values of the ground truth and prediction, respectively.  $\text{cov}(\hat{x}_i, x_i)$  is the covariance between  $\hat{x}_i$  and  $x_i$ .  $\sigma_{\hat{x}_i}$  and  $\sigma_{x_i}$  are the standard deviations of  $\hat{x}_i$  and  $x_i$ , respectively.

## III. RESULTS AND DISCUSSIONS

The models are implemented in Python with the PyTorch package and trained on a server with two 12GB NVIDIA TITAN GPUs, dual 10-core Intel(R) Xeon(R) Silver 4114 CPUs @ 2.20GHz, and 251 GB of RAM. In this study, the Adam optimizer is employed [26]. The Leaky rectified linear unit (ReLU) activation function with a leaky value of 0.2 is used to avoid dead neurons in the networks caused by

conventional ReLU due to the “dying ReLU problem” [27]. Batch normalization is implemented to accelerate training by reducing internal covariate shift [21]. Dropout regularization is used to reduce overfitting and to improve the model generalization ability [22]. The learning rate and batch size are set to 5e-5 and 72 based on trial-and-error runs, respectively.

Four convLSTM-based models with different combinations of loss functions ( $L_1$  and  $L_2$ ) and prediction strategies (direct and residual predictions, see details in subsection II-B) are implemented. These four models are shown in Table II.

Table III shows performance comparison of the four models on training, validation and testing sets, respectively. Model C has the best performance with lower  $RMSE$  and  $MAE$  values and higher  $CC$  values compared to the other three models on all data sets. This may be due to two reasons. First, the  $L_1$  loss is capable of forcing the model to obtain accurate predictions that are far away from the mean values, which is especially helpful for predicting TEC values with large magnitudes, such as the TEC peaks around the local noon sector and equatorial ionization anomaly (EIA) crest regions. Second, the utilization of residual prediction strategy removes the background ionosphere, forcing the model to only focus on the smaller range associated with deviations of the ionosphere. Because of the better performance of model C, ML prediction results and performances discussed in the remaining paper are all obtained from model C. In the remaining paper, the convLSTM refers to model C.

### A. A Qualitative Case Study

In this case study, we compare the convLSTM prediction with that of c1pg during the main phase of a storm event that occurred during 10:00-13:00 UT on May 6, 2015, when  $KP \approx 3 - 5.3$  and  $F10.7=138.6$ . The c1pg is 1-day predicted global ionospheric TEC map released by CODE analysis center, and it is produced based on the extrapolation of spherical harmonic coefficients [7]. Figure 4 shows the 1-hour interval TEC maps predicted by the convLSTM and c1pg models. The codg refers to CODE’s GIM, which is the ground truth. The plots show that the predicted TEC maps from convLSTM and c1pg agree well with the truth. In particular, large-scale ionospheric patterns, such as the daytime EIA crests, are well-preserved. We can also observe from Figure 4 that the predicted TEC maps from convLSTM are closer to the truth than those from c1pg. For example, The TEC enhancement shown near  $30^{\circ}\text{E}-80^{\circ}\text{E}$  longitude and  $40^{\circ}\text{S}-60^{\circ}\text{S}$  latitude of codg is well reproduced in the convLSTM model (see red circles in the middle column of Figure 4), while the c1pg fails to capture it.

Figure 5 shows the difference between the truth and predicted maps during the main phase of the storm event. The magnitude of the TEC difference maps from convLSTM is clearly smaller than that from c1pg. This indicates the convLSTM ML model has a better prediction performance than c1pg. In addition, an example during geomagnetic quiet time also corroborates the same conclusion that the convLSTM has a better performance (see Figure S2 and Movie S2 in the SI).

TABLE I  
DETAILED PARAMETER CONFIGURATIONS OF THE MODEL ARCHITECTURE. I AND O REPRESENT INPUT AND OUTPUT OF EACH MODULE, RESPECTIVELY.

Network	Module	Filter number		Filter size	Stride	Padding	Height and width	
		I	O				I	O
Encoder	conv	1	8	3x3	2x2	1x1	73x73	37x37
	convLSTM	8	16	5x5	1x1	2x2	37x37	37x37
	conv	16	16	3x3	2x2	1x1	37x37	19x19
	convLSTM	16	32	5x5	1x1	2x2	19x19	19x19
	conv	32	32	3x3	2x2	1x1	19x19	10x10
	convLSTM	32	32	5x5	1x1	2x2	10x10	10x10
Decoder	convLSTM	32	32	5x5	1x1	2x2	10x10	10x10
	deconv	32	32	3x3	2x2	1x1	10x10	19x19
	convLSTM	32	32	5x5	1x1	2x2	19x19	19x19
	deconv	32	32	3x3	2x2	1x1	19x19	37x37
	convLSTM	32	16	5x5	1x1	2x2	37x37	37x37
	deconv	16	8	3x3	2x2	1x1	37x37	73x73
	conv	8	1	1x1	1x1	0x0	73x73	73x73

TABLE II  
FOUR CONVLSTM-BASED MODELS IMPLEMENTED IN THIS STUDY BY COMBINING DIFFERENT LOSS FUNCTIONS AND PREDICTION STRATEGIES.

Model	Loss function	Prediction strategy
A	$L_1$	direct prediction
B	$L_2$	direct prediction
C	$L_1$	residual prediction
D	$L_2$	residual prediction

### 252 B. Statistical Evaluation

253 A statistical evaluation is also conducted under varying levels  
254 of solar and geomagnetic activities. The convLSTM is com-  
255 pared to c1pg and to a persistence model. The persistence  
256 model assumes that the predicted TEC map at time t is the  
257 same as that at t-24. F10.7 and KP parameters are used as  
258 indicators of solar and geomagnetic levels, respectively. Table  
259 IV shows the definitions of the high/low solar activity and  
260 geomagnetic storm/quiet levels.

261 Figure 6 shows comparison results under low (a) and high  
262 (b) solar activities on the testing set as functions of the lead  
263 time. Four metrics are plotted for each solar activity level. The  
264 following observations are obtained:

265 (1) The convLSTM model shows better prediction perfor-  
266 mance compared to c1pg and persistence models for all lead  
267 times and with all metrics.

268 (2) A slight performance degradation is observed for convL-  
269 STM under high solar activities compared to the ones under  
270 low solar activities. For example, the RMSE increases from  
271 1.78 to 3.31 TECU. Such levels of prediction error difference  
272 are within the margin of the truth precision, which is around  
273 2-8 TECU [8], [28], [29].

274 (3) The predictive capability of the convLSTM degrades with  
275 increasing lead time, while c1pg and persistence models show  
276 almost no dependence on the lead time.

277 Figure 7 compares the performance using data collected under  
278 geomagnetic quiet (a) and storm (b) conditions. We have the

following observations:

(1) The convLSTM model shows better performance compared  
281 to other two models for all lead times tested under geomag-  
282 netic quiet conditions.

(2) During geomagnetic storms, the prediction performance of  
283 the convLSTM remains the best when the lead time is smaller  
284 than 8 hours. The c1pg shows a slightly better performance  
285 compared to convLSTM when the lead time is longer than 8  
286 hours, and there is a notable performance improvement with  
287 increasing lead time under geomagnetic storm conditions. Ad-  
288 ditional investigations may be required to study this behavior.

(3) For the convLSTM model, the minimum RMSE errors  
290 for quiet/storm time are 0.81/1.28 TECU, and the maximum  
291 RMSE errors for quiet/storm time are 2.15/3.26 TECU. This  
292 indicates that the RMSE degradation of convLSTM is not  
293 significant under geomagnetic storm conditions. Similar ob-  
294 servations can be found from other metrics. This may be due  
295 to the fact that some features from geomagnetic activities  
296 have already been contained in the 24 input TEC maps  
297 of the convLSTM model, thus leading to an insignificant  
298 performance degradation under storm conditions.

Figure 8 plots the ME (top panel) and RMSE (bottom panel)  
300 errors of the convLSTM, c1pg and persistence models as func-  
301 tions of latitude. The convLSTM has the smallest ME error.  
302 Moreover, the ME errors of the convLSTM and persistence  
303 model stabilize around zero across all latitudes. This indicates  
304 that there are no systematic biases in the TEC maps predicted  
305 by convLSTM and the persistence models. However, c1pg  
306 underestimates/overestimates the predicted TEC over the mid-  
307 high latitude of the southern/northern hemispheres. In terms of  
308 RMSE errors, the convLSTM shows an improved performance  
309 over the other two models over various latitudes. In addition,  
310 the RMSE errors of three models show obvious latitudinal de-  
311 pendence, and two peaks are located near geographic latitude  
312 of 10°S and 20°N, respectively. This is probably related to  
313 strong ionospheric gradients around the daily EIA crest.

TABLE III  
DETAILED PARAMETER CONFIGURATIONS OF THE MODEL ARCHITECTURE. I AND O REPRESENT INPUT AND OUTPUT OF EACH MODULE, RESPECTIVELY.

Model	RMSE (TECU)			MAE (TECU)			CC		
	Train	Validation	Test	Train	Validation	Test	Train	Validation	Test
A	1.90	1.97	1.94	1.22	1.25	1.24	0.97	0.97	0.96
B	2.0	2.03	2.01	1.34	1.35	1.33	0.96	0.96	0.96
C	1.72	1.90	1.88	1.12	1.20	1.20	0.98	0.97	0.97
D	2.06	2.04	2.03	1.35	1.33	1.33	0.96	0.97	0.96

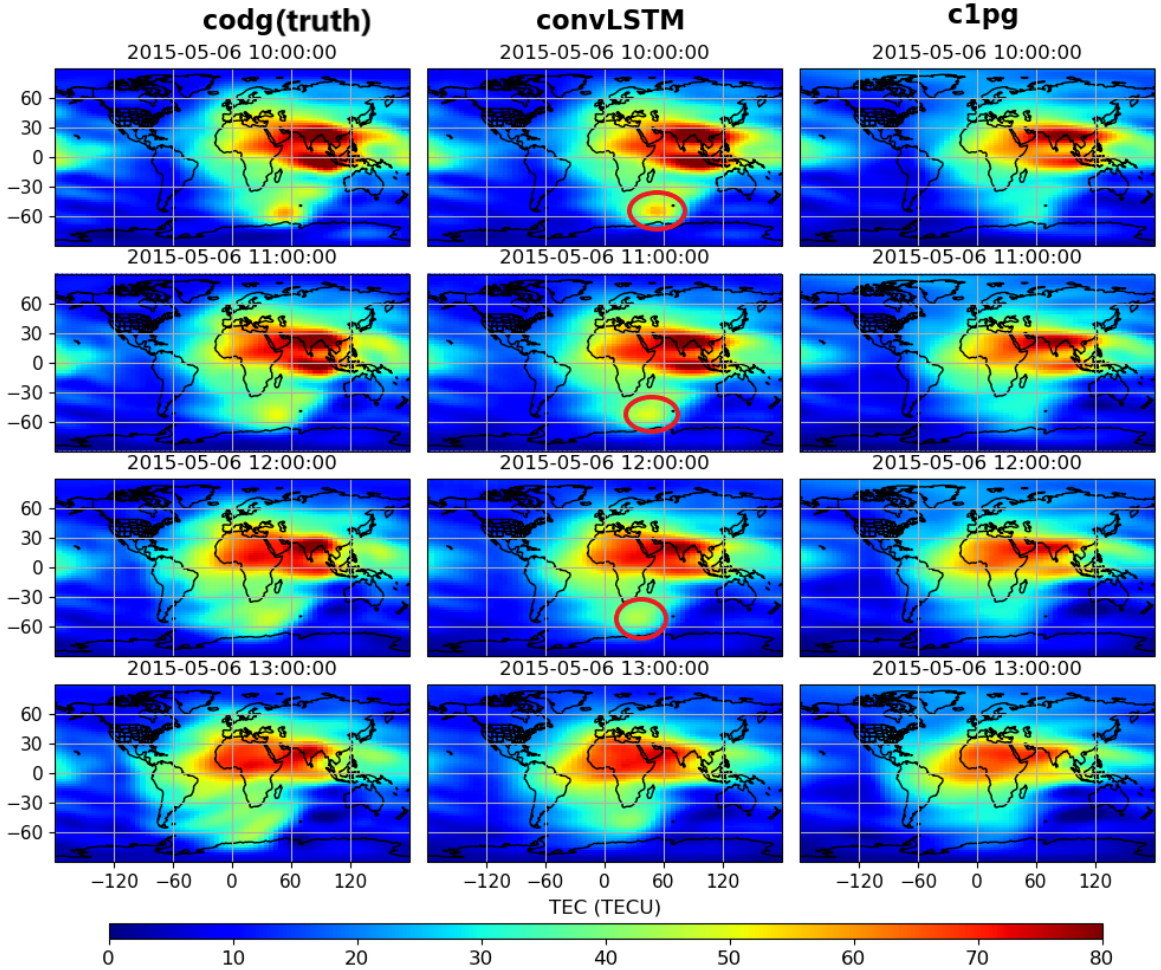


Fig. 4. An example of the predicted global TEC maps at a 1-hour interval during the main phase of one geomagnetic storm event (10:00-13:00 UT, May 6, 2015), where the KP varies from 3.7 to 5.3, and F10.7 is 138.6. The left column represents the TEC maps from codg, which are the ground truth. The middle and right columns represent the predicted TEC maps from convLSTM and c1pg, respectively. Full sets of the predicted global TEC maps with lead times up to 24 hours are available in Movie S1 of the SI.

TABLE IV  
THE THRESHOLD OF DIFFERENT SOLAR AND GEOMAGNETIC ACTIVITY LEVELS.

Indicators	Threshold	Defined levels
F10.7	$F10.7 \geq 120$	high solar activity
	$F10.7 < 120$	low solar activity
KP	$KP > 4$	geomagnetic storm
	$KP < 4$	geomagnetic quiet

315

#### IV. CONCLUSIONS

316 This paper discusses convLSTM-based ML algorithms imple-  
317 mented to predict daily global TEC maps using CODE data

318 collected from October 19, 2014 to July 21, 2021. Among  
319 four different implementations, the convLSTM model that  
320 combines the  $L_1$  loss function and residual prediction strategy  
321 shows the best performance. This best performing convLSTM  
322 model also shows more accurate prediction compared to  
323 c1pg, which is 1-day predicted global TEC product released  
324 by CODE analysis center. Moreover, prominent structures,  
325 such as typical EIA and TEC enhancement over southern  
326 hemisphere, are successfully reproduced by the convLSTM  
327 model.

328 Our statistical evaluation shows that the convLSTM model  
329 significantly outperforms both the c1pg and persistence models

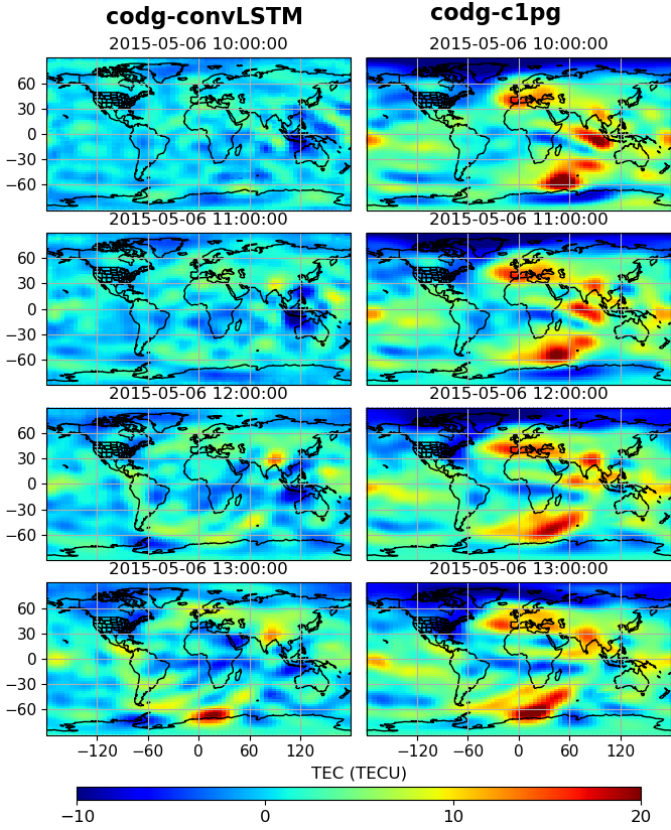


Fig. 5. Comparison of the TEC difference maps between codg and convLSTM. Left column: codg minus convLSTM. Right column: codg minus c1pg.

under all levels of solar activities for all lead times tested and at all latitudes. A slight performance degradation is observed for convLSTM under high solar activities compared to the ones under low solar activities. When compared to c1pg and persistence models, the convLSTM model shows better performance for all lead times tested under geomagnetic quiet conditions and for lead times below 8 hours of storm conditions. For lead times beyond 8 hours during the storm times, the c1pg has slightly better performance. The convLSTM model shows an insignificant performance degradation during the storm time compared to the quiet time. The convLSTM model degrades with the increasing lead time, while only a very weak time dependence is observed in results from the c1pg and persistence models.

344

#### ACKNOWLEDGMENT

This project is sponsored by DARPA DSO Space Environment Exploitation (SEE) Program grant #DI 9AC00009. The CODE GIM data are available from the Crustal Dynamics Data Information System (CDDIS) (<https://cddis.nasa.gov/>) via registration. Solar and Geomagnetic data are obtained from the OMNI Goddard Flight Center (<https://omniweb.gsfc.nasa.gov/>). The authors acknowledge the SWAMI server at the Space Weather Technology, Research and Education Center (SWx-TREC), University of Colorado, Boulder for providing high-performance computing that contributed to this work.

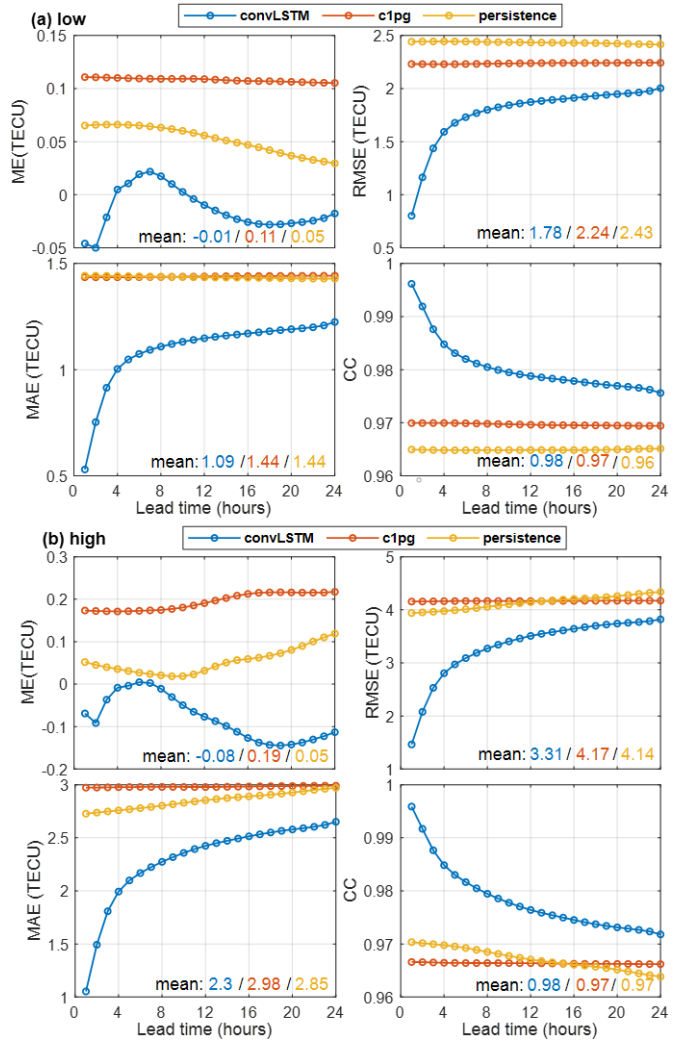


Fig. 6. Performance comparison among convLSTM, c1pg, and the persistence models under the low (a) and high (b) solar activity levels on the testing set. Blue, red, and orange curves in each panel refer to metrics obtained from convLSTM, c1pg, and persistence models, respectively. Mean metrics across all lead time are illustrated at the bottom of each panel.

#### REFERENCES

- [1] S. Basu, S. Basu, E. MacKenzie, W. Coley, J. Sharber, and W. Hoegy, “Plasma structuring by the gradient drift instability at high latitudes and comparison with velocity shear driven processes,” *Journal of Geophysical Research: Space Physics*, vol. 95, no. A6, pp. 7799–7818, 1990.
- [2] K. C. Yeh and C.-H. Liu, “Radio wave scintillations in the ionosphere,” *Proceedings of the IEEE*, vol. 70, no. 4, pp. 324–360, 1982.
- [3] K. S. Jacobsen and Y. L. Andalsvik, “Overview of the 2015 st. patrick’s day storm and its consequences for rtk and ppp positioning in norway,” *Journal of Space Weather and Space Climate*, vol. 6, p. A9, 2016.
- [4] J. A. Klobuchar, “Ionospheric time-delay algorithm for single-frequency gps users,” *IEEE Transactions on aerospace and electronic systems*, no. 3, pp. 325–331, 1987.
- [5] N. Jakowski, Y. Béniguel, G. De Franceschi, M. H. Pajares, K. S. Jacobsen, I. Stanislawska, L. Tomaszik, R. Warnant, and G. Wautlet, “Monitoring, tracking and forecasting ionospheric perturbations using gnss techniques,” *Journal of Space Weather and Space Climate*, vol. 2, p. A22, 2012.
- [6] Y. J. Morton, Z. Yang, B. Breitsch, H. Bourne, and C. Rino, “Ionospheric effects, monitoring, and mitigation techniques,” *Position, Navigation, and Timing Technologies in the 21st Century: Integrated Satellite*

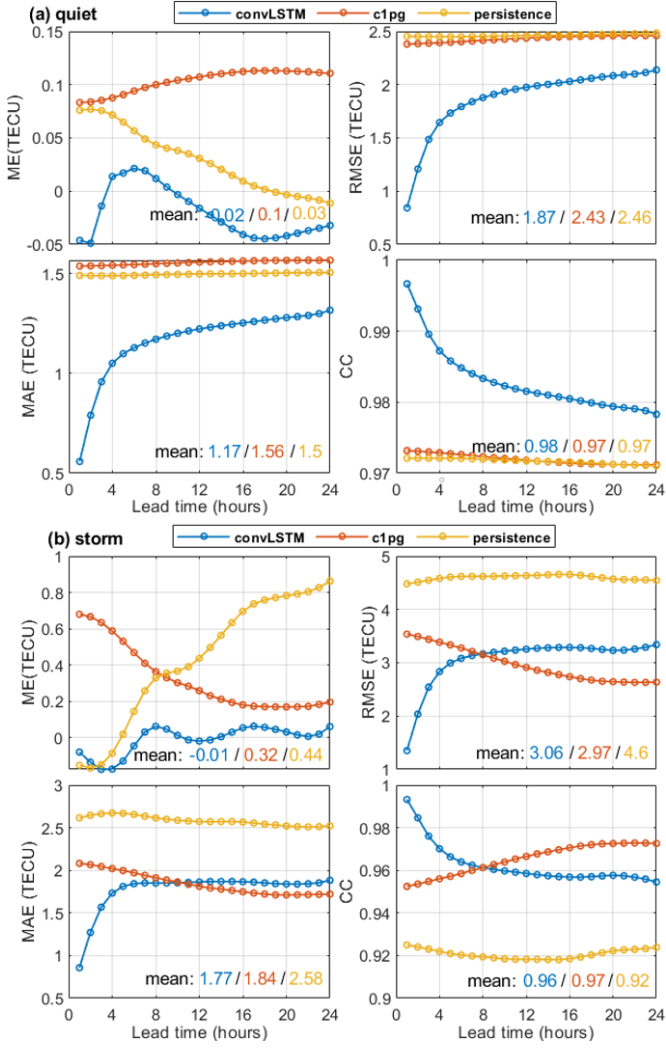


Fig. 7. Performance comparison among convLSTM, c1pg, and persistence models under geomagnetic quiet (a) and storm levels (b) on the testing set.

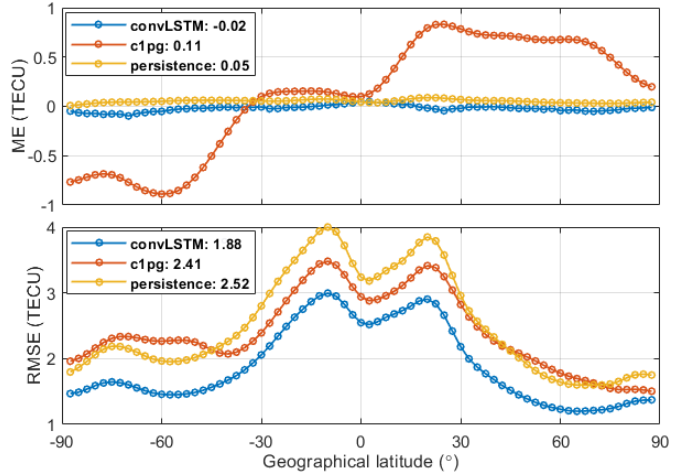


Fig. 8. Latitudinal ME (top panel) and RMSE (bottom panel) errors of three prediction models on the testing set. Blue, red and orange curves represent evaluations metrics from convLSTM, c1pg and persistence models, respectively. The average ME and RMSE values of each model across all latitude are shown in the legend.

- [13] E. Camporeale, "The challenge of machine learning in space weather: Nowcasting and forecasting," *Space Weather*, vol. 17, no. 8, pp. 1166–1207, 2019. 399  
400  
401
- [14] L. Liu, S. Zou, Y. Yao, and E. Aa, "Multi-scale ionosphere responses to the may 2017 magnetic storm over the asian sector," *GPS Solutions*, vol. 24, no. 1, pp. 1–15, 2020. 402  
403  
404
- [15] A. García-Rigo, E. Monte, M. Hernández-Pajares, J. Juan, J. Sanz, A. Aragón-Angel, and D. Salazar, "Global prediction of the vertical total electron content of the ionosphere based on gps data," *Radio science*, vol. 46, no. 06, pp. 1–3, 2011. 405  
406  
407  
408
- [16] C. Wang, S. Xin, X. Liu, C. Shi, and L. Fan, "Prediction of global ionospheric vtec maps using an adaptive autoregressive model," *Earth, Planets and Space*, vol. 70, no. 1, pp. 1–14, 2018. 409  
410  
411
- [17] R. O. Perez, "Using tensorflow-based neural network to estimate gnss single frequency ionospheric delay (iononet)," *Advances in Space Research*, vol. 63, no. 5, pp. 1607–1618, 2019. 412  
413  
414
- [18] S. Lee, E.-Y. Ji, Y.-J. Moon, and E. Park, "One-day forecasting of global tec using a novel deep learning model," *Space Weather*, vol. 19, no. 1, p. 2020SW002600, 2021. 415  
416  
417
- [19] L. Liu, S. Zou, Y. Yao, and Z. Wang, "Forecasting global ionospheric tec using deep learning approach," *Space Weather*, vol. 18, no. 11, p. e2020SW002501, 2020. 418  
419  
420
- [20] A. Boulch, N. Cherrier, and T. Castaings, "Ionospheric activity prediction using convolutional recurrent neural networks," *arXiv preprint arXiv:1810.13273*, 2018. 421  
422  
423
- [21] S. Ioffe and C. Szegedy, "Batch normalization: Accelerating deep network training by reducing internal covariate shift," in *International conference on machine learning*. PMLR, 2015, pp. 448–456. 424  
425  
426
- [22] S. Wager, S. Wang, and P. S. Liang, "Dropout training as adaptive regularization," *Advances in neural information processing systems*, vol. 26, pp. 351–359, 2013. 427  
428  
429
- [23] S. Xingjian, Z. Chen, H. Wang, D.-Y. Yeung, W.-K. Wong, and W.-c. Woo, "Convolutional lstm network: A machine learning approach for precipitation nowcasting," in *Advances in neural information processing systems*, 2015, pp. 802–810. 430  
431  
432  
433
- [24] X. Shi, Z. Gao, L. Lausen, H. Wang, D.-Y. Yeung, W.-k. Wong, and W.-c. Woo, "Deep learning for precipitation nowcasting: A benchmark and a new model," *arXiv preprint arXiv:1706.03458*, 2017. 434  
435  
436

- 437 [25] L. Liu, Y. J. Morton, and Y. Liu, "Machine learning prediction  
 438 of storm-time high-latitude ionospheric irregularities from gnss-  
 439 derived roti maps," *Geophysical Research Letters*, vol. 48, no. 20, p.  
 440 e2021GL095561, 2021.
- 441 [26] D. P. Kingma and J. Ba, "Adam: A method for stochastic optimization,"  
 442 *arXiv preprint arXiv:1412.6980*, 2014.
- 443 [27] B. Xu, N. Wang, T. Chen, and M. Li, "Empirical evaluation of rectified  
 444 activations in convolutional network," *arXiv preprint arXiv:1505.00853*,  
 445 2015.
- 446 [28] Z. Li, Y. Yuan, N. Wang, M. Hernandez-Pajares, and X. Huo, "Shpts:  
 447 towards a new method for generating precise global ionospheric tec  
 448 map based on spherical harmonic and generalized trigonometric series  
 449 functions," *Journal of Geodesy*, vol. 89, no. 4, pp. 331–345, 2015.
- 450 [29] D. Roma-Dollase, M. Hernández-Pajares, A. Krancowski, K. Kotulak,  
 451 R. Ghoddousi-Fard, Y. Yuan, Z. Li, H. Zhang, C. Shi, C. Wang  
 452 *et al.*, "Consistency of seven different gnss global ionospheric mapping  
 453 techniques during one solar cycle," *Journal of Geodesy*, vol. 92, no. 6,  
 454 pp. 691–706, 2018.

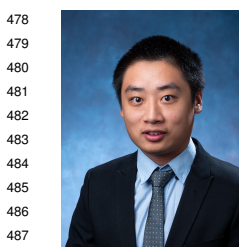


455 **Lei Liu** is a Post-Doc Research Associate for the  
 456 Satellite Navigation and Sensing Laboratory at the  
 457 University of Colorado Boulder. He received his  
 458 Ph.D. in Geodesy and Geomatics from Wuhan Uni-  
 459 versity China in 2020. His current research interests  
 460 are GNSS ionospheric monitoring, modeling, and  
 461 forecasting of ionospheric TEC and irregularities  
 462 using machine learning.

463



464 **Dr. Y. Jade Morton** is the Helen and Hubert Croft  
 465 Professor of Engineering in the Smead Aerospace  
 466 Engineering Sciences Department at the University  
 467 of Colorado (CU), Boulder. Her research interests lie  
 468 at the intersection of satellite navigation technolo-  
 469 gies and remote sensing of the Earth's ionosphere,  
 470 atmosphere, and surface. Dr. Morton received her  
 471 PhD in electrical engineering from Penn State and  
 472 was an electrical engineering professor at Colorado  
 473 State University and Miami University prior to join  
 474 CU in 2017. Dr. Morton is an Institute of Navigation  
 475 (ION) Thurlow, Burk and Kepler award winner, an IEEE PLANS Kershner  
 476 award winner, and an IEEE AESS Distinguished Lecturer. She is a fellow of  
 477 IEEE, the ION, and the Royal Institute of Navigation (RIN).



478 **Yunxiang Liu** obtained the PhD from Aerospace  
 479 Engineering Sciences at the University of Colorado  
 480 Boulder. He received a B.E. at the University of  
 481 Electronic Science and Technology of China in 2013  
 482 and an M.E. Degree from Nanyang Technological  
 483 University (NTU) in 2015, both majoring in wireless  
 484 communications. He worked on machine learning re-  
 485 lated problems as a research associate at NTU from  
 486 2015 to 2016, and later at the Rolls-Royce@NTU  
 487 Corporate Lab from 2016 to 2017. His research work  
 488 focuses on applying machine learning techniques to  
 489 GNSS-based remote sensing tasks.